

Synthetic observations of highly clumped formation of CO and C I clouds in the
turbulent interstellar medium; Implications on the seed CO clouds and the CO-dark
H₂ gas

KENGO TACHIHARA,¹ YASUO FUKUI,¹ TAKAHIRO HAYAKAWA,¹ AND
TSUYOSHI INOUE¹

¹*Department of Physics, Nagoya University, Chikusa-ku Nagoya 464-8602, Japan*

(Received; Revised; Accepted)

Submitted to

ABSTRACT

We carried out synthetic observations of a theoretical model of interstellar carbon in CO, C I and C II including H₂ formation. The theoretical model based on numerical simulations of H I gas converging at a velocity of 20 km s⁻¹ by Inoue & Inutsuka (2012) is employed in the present study. The gas model, which is fairly realistic and consistent with the observations of the local gas located at high b , is turbulent and inhomogeneous with magnetic field. We focus on the evolution of the rare species, CO, C I and C II from 0.3 Myr to 9 Myr since the converging flows collided. In the early phase within 1 Myr, the Cold Neutral Medium (CNM) clumps of sub-pc scales are the formation sites of H₂, CO and C I, and in the late phase from 3 Myr to 9 Myr the CNM clumps merge together to form pc-scale molecular clouds. The results show that C I and CO are well mixed at pc scales, and mark a significant disagreement with the classic picture which predicts layered C I and CO distributions according to A_V . We suggest that the faint CO clouds in the Oph North (Tachihara et al. 2012) and the Pegasus loop (Yamamoto et al. 2006) are promising candidates for such small CO clouds. The total mass budget of the local ISM indicates the fraction of H I is about 70% and the CO-dark H₂ is small, less than a few percent, contrary to the usual assumption.

1. INTRODUCTION

The interstellar medium (ISM) plays an important role in galactic evolution by forming stars. A detailed study of the ISM is possible only for the local ISM which is distributed within 300 pc of the sun, where no giant molecular clouds (GMCs) forming

high mass stars are found. The present work focuses on the local ISM whose peak H column density is $\sim 10^{21} \text{ cm}^{-2}$. The local gas is relatively diffuse and contains little CO clouds except for dark clouds including Taurus, Chameleon, R CrA, etc.

The interstellar molecular clouds are the almost exclusive site of star formation. As an evolutionary step prior to star formation, molecular cloud formation is an important process in galaxy evolution, and considerable efforts have been devoted to better understanding molecular cloud formation in the previous studies (for a recent review see [Dobbs et al. 2014](#), and references therein). Our understanding on cloud formation is yet preliminary both theoretically and observationally and more efforts are to be made toward confronting theories and observations and to acquire comprehensive understanding of the physical and chemical processes and their observable signatures.

Some theoretical works were made aiming at understanding formation of the molecular clouds at various scales from sub-pc to kpc ([Dobbs et al. 2014](#)). The aim of the present work is to better understand the formation process at 0.02 pc to 10 pc scales by incorporating the micro physical processes including photoelectric heating and atomic and molecular cooling, cosmic ray ionization, molecular formation of H₂ and CO, and the interstellar radiation field and cosmic rays. For the purpose, we employ one of the most advanced numerical simulations of the realistic ISM having highly turbulent inhomogeneous distribution with magnetic field.

Since we are interested in the behavior of carbon bearing species, the role of the radiation field is crucial. The effects of the UV radiation appear as regions with diverging ionization states which are governed by A_V under a given radiation field. A pioneering work by [Tielens & Hollenbach \(1985\)](#) developed the photo dissociation region (PDR) model, where the ISM is exposed to external UV radiation field of various intensity. Carbon behavior, the major constituent of the ISM, attracted a broad interest and a number of theoretical simulations were undertaken previously (e.g. [Glover et al. 2010](#)). Most of these studies were made for uniform or non-uniform but smooth, density distribution. The results predicted that the C II, C I and CO are distributed in layers in a sequence of A_V ([Tielens & Hollenbach 1985](#)). For small A_V less than 0.3 mag, C II is dominant and C I increases with A_V .

The observations of C I are not so plentiful. Large scale C I observations were made with the Mt. Fuji sub-mm telescope and provided C I distribution in nearby clouds including Taurus, Orion, etc. ([Maezawa et al. 1999](#); [Ikeda et al. 1999](#); [Oka et al. 2001](#); [Kamegai et al. 2003](#)). Their results showed that C I and CO distributions are fairly similar and the distinct difference as predicted by the PDR model was not observed. [Glover et al. \(2015\)](#) proposed highly turbulent field in the ISM in order to solve the discrepancy and showed that the turbulence can introduce more UV photons deeply into a cloud, and thereby realizes ionization over a cloud, producing similar C I and CO distributions.

The aim of the present work is to clarify the behavior of the ISM in particular the observed properties of the CO and C I and their relationship with the density distribution of the ISM. For the purpose, we employ the converging H I flow model by [Inoue & Inutsuka \(2012\)](#). This model is distinguished from others which assume high density as the initial condition; e.g., [Glover & Mac Low \(2007\)](#) assumes uniform and static H I with density = 100 cm^{-2} as the initial condition, which excludes the Warm Neutral Medium (WNM). [Fukui et al. \(2018\)](#) used the model by [Inoue & Inutsuka \(2012\)](#) and synthesized H I and H₂ distributions. These authors showed that the Cold Neutral Medium (CNM) has a highly clumpy distribution with a volume filling factor of 3.5% which is consistent with the observations. The present paper makes synthetic observations of CO and C I which are included in the same model, and aims to gain better insight into the interstellar carbon behavior. Section 2 gives the model description, and Section 3 presents details of the results. Discussion is given in Section 4, and Section 5 summarizes the conclusions.

2. MODELS AND THE SYNTHETIC OBSERVATIONS

The present simulations of the converging H I flows at 20 km s^{-1} were made by [Inoue & Inutsuka \(2012\)](#), and adopt initial conditions which consider the realistic inhomogeneous density distribution as a natural consequence of the thermal instability based on magneto-hydrodynamical code. Heating by the background FUV field and cosmic rays are taken into account as well as molecular and atomic coolings. Chemical reactions including those relevant to H⁺, H₂, CO, C I and C II are considered. More details are found in [Inoue & Inutsuka \(2012\)](#). All the datasets have pixels of 512^3 for a length of 20 pc in each axis. The following four models are used in the present study, while usually we showed the results of Model A in the present paper.

Model A is based on the numerical simulations which were employed in [Fukui et al. \(2018\)](#), where the H I flows continuously enter into the simulation box at 20 km s^{-1} from the both sides along the x -axis. Magnetic field is assumed to be parallel to the x -axis, so that the converging flows compressed very efficiently to form molecular cloud taking 10 Myr. See more details in [Inoue & Inutsuka \(2012\)](#).

Unlike Model A, Models B, C, and D make the H I flows injected from both sides along the x -axis collide only once around $x = 10 \text{ pc}$. Model B assumes the initial velocity as follows;

$$V_x (\text{km s}^{-1}) = \frac{5x}{(\text{pc})} \quad (\text{for } x < 10 \text{ pc}),$$

$$V_x (\text{km s}^{-1}) = \frac{5x}{(\text{pc})} - 100 \quad (\text{for } x > 10 \text{ pc}).$$

This setup allows us to simulate that the ISM in the numerical domain is compressed by the shock and after that the increased pressure of the ISM is taken back to an average value of the ISM due to the cooling (in contrast, the shock compressed region in Model A keeps high thermal pressure because the converging flows are continuously

set at the boundary). With this initial velocity field, the total kinetic energy of $\sim 2 \times 10^{49}$ erg is injected into the numerical domain of 20 pc^3 volume, which is comparable to that given by a supernova explosion. The field direction is taken at 45 degrees relative to the x -axis in the x - y plane, while Model A assumed this angle to be 0 degrees.

Model C has smaller initial velocity as follows;

$$V_x (\text{km s}^{-1}) = \frac{2x}{(\text{pc})} \text{ (for } x < 10 \text{ pc),}$$

$$V_x (\text{km s}^{-1}) = \frac{2x}{(\text{pc})} - 40 \text{ (for } x > 10 \text{ pc).}$$

Model D has the initial velocity same as Model C, but the field direction is taken in the x -axis.

Synthetic CO, C I and C II profiles were calculated by using a line radiation transfer code RADMC-3D (Dullemond et al. 2012). The code first computes the level populations consistent with the local density, temperature and velocity field by adopting the Large Velocity Gradient (LVG) method (also known as ‘‘Sobolev approximation’’), and then performs a ray-tracing line transfer calculation with the derived level population. The molecular/atomic data required for the calculations (energy levels, the Einstein A coefficients and rate coefficients of collisional excitation/de-excitation) are taken from Leiden Atomic and Molecular Database (LAMDA) (Schöier et al. 2005).

3. RESULTS

3.1. Density and temperature distribution

Figure 1 shows distributions of density and temperature for Model A at 0.5 Myr (reproduced from Fukui et al. 2018). The gas temperature ranges from 10 K to 10^4 K, where the WNM and CNM have a boundary at 300 K, and density ranges from 1 to 10^4 cm^{-3} . The mass ratio of the two phases are $\sim 4 : 6$ for the CNM and WNM. The pressure distributions for the present 4 models at 0.5 Myr are shown as a function of density in Figure 2, where two stratified gas components corresponding to the WNM and CNM are seen. The pressure range is also quite broad from $\sim 10^3 \text{ K cm}^{-3}$ to $\sim 10^6 \text{ K cm}^{-3}$, because the medium is far from the dynamical equilibrium at a uniform pressure. This is characteristics to the highly turbulent state, and causes a number of transient structures of H I in the order of 10^4 yr as shown later. Small differences between the 4 models can be seen in Figure 2. Model A makes higher pressure of the WNM caused by the continuous gas flow than the other 3 models. On the other hand, the pressure and density of CNM do not vary a lot among the different models. Thus the different model setups causes little effects on the results of the chemical characteristics, mass ratio, and the volume filling factors of the CNM.

3.2. Relative abundance of carbon-bearing species, CO, C I and C II

Figure 3 shows density and relative abundance of H₂, CO, C I, and C II as a function of total density in Model A at 0.5 Myr and 3.0 Myr. In Figure 3 majority of hydrogen is in H I, and H₂ is about 0.01–0.1 of H I in number. The amount of H II is negligibly small. Model A at 0.5 Myr, among the various epochs of Model A, matches best the UV absorption measurements of H₂ abundance and N_{HI} in the local interstellar medium (Fukui et al. 2018). At 0.5 Myr, CO is a minor constituent with abundance of $\sim 10^{-10}$ at low density around 100 cm^{-3} , while it grows with density to 10^{-6} at density above 10^3 cm^{-3} . At the highest density around $(2-5) \times 10^3 \text{ cm}^{-3}$, CO abundance of $\sim 10^{-4}$, close to the total C abundance, is reached in a small number of pixels. C I shows an abundance increase from 10^{-7} to 10^{-5} with density in the same density range, and this variation is smaller than in CO. C II shows fairly uniform abundance of $\sim 10^{-4}$ and does not depend on density. Only at the highest end of $(2-5) \times 10^3 \text{ cm}^{-3}$ C II abundance shows slightly larger dispersion, which is due to net conversion of C II into CO. Table 1 presents a summary of the relative abundances of the species along with the CNM volume filling factor of the models.

Figure 4 shows time evolution of abundance of the four species of Model A measured at 10^3 cm^{-3} at epochs from 0.3 Myr to 9.0 Myr. Abundance of H₂, CO and C I increases in time via chemical reactions including H₂ formation and due to the increase in shielding by the increase in N_{H} and A_{V} . Almost full conversion of H I into H₂ is seen at 9 Myr, while H I is always dominant at epochs younger than 6 Myr. This dominance of H I is not observed in the previous models, which for instance adopted the initial condition that H I has high uniform density = 100 cm^{-3} and static velocity field (Glover & Mac Low 2007). In Model A CO abundance shows a steep gradient in time from less than 10^{-6} to 10^{-4} over the time range. The Model A at 9 Myr represents a mature molecular cloud which has H₂ and CO relative abundance of 1.0 and 10^{-4} , respectively.

Figure 5 shows spatial distribution of the four quantities in Model A at three epochs, 0.5, 1.0 and 3.0 Myr. The quantities are total hydrogen column density $N_{\text{HI}} + 2N_{\text{H}_2}$, the total velocity integrated intensity of the CO $J = 1-0$ emission at 115.2712018 GHz W_{CO} , that of C I $^3\text{P}_1-^3\text{P}_0$ emission at 492.160651 GHz W_{CI} , and that of C II $^2\text{P}_{3/2}-^2\text{P}_{1/2}$ emission at $157.7409 \mu\text{m}$ W_{CII} . The distributions show marked difference between 0.5 and 1.0 Myr vs. 3.0 and 6.0 Myr. In the early epochs the distributions are largely dominated by small clumps, while in the latter epochs the emission becomes more continuous and organized into larger aggregations. We present an interpretation of this trend as signatures of molecular cloud formation in Section 4. We note that the distribution is highly transient in a typical timescale of 10^4 yr , and any hysteresis in the Model is rapidly lost within that time scale.

Two sightlines are chosen rather arbitrarily in Figure 5 and the strip maps of density and abundance are shown in the sightlines in Figure 6 at two epochs, 0.5 Myr and 3.0 Myr. This allows us to see the detailed variation in space. Figure 6(a)-1 shows an early phase of evolution at 0.5 Myr and shows dense clumps as sharp spikes with

highest H_2 density above 10^2 cm^{-3} at four positions, $y = 2.7 \text{ pc}$, 4.6 pc , 5.5 pc and 7.1 pc , where the one close to the edge, $y = 0.1 \text{ pc}$, is excluded. The clumps have peak density of $100\text{--}500 \text{ cm}^{-3}$. Figure 6(b)-1 shows abundance of four species, H_2 , C II, C I and CO. H_2 abundance is peaked at 10^{-1} toward the two densest clumps, the 3rd and 4th, and the 2nd and 1st clumps have H_2 abundance of $\sim 7 \times 10^{-2}$ and $\sim 10^{-3}$, respectively. In Figure 6(b)-1 C II abundance is quite uniform at 10^{-4} , and C I abundance shows moderate variation from 10^{-8} to 10^{-6} . Compared to these, the CO abundance changes significantly from less than 10^{-20} to 10^{-7} , showing maximum values toward the 3rd and 4th clumps. Figure 6(a)-2 shows a later phase at 3 Myr in the same sightline. We find two outstanding regions with enhanced H_2 density at $y = 0.8\text{--}3.0 \text{ pc}$ and $7.5\text{--}9.5 \text{ pc}$, which have H_2 abundance greater than 0.1. The general behavior of the four species is similar to the epoch of 0.5 Myr. The CO abundance is significantly increased to $10^{-10}\text{--}10^{-6}$ at 3.0 Myr.

3.3. Synthetic observations of CO, C I and C II

Figures 7(a), (b) and (c) show scatter plots between W_{CO} vs. $N_{\text{HI}} + 2N_{\text{H}_2}$, W_{CI} vs. $N_{\text{HI}} + 2N_{\text{H}_2}$ and W_{CO} vs. W_{CI} . The distributions of W_{CO} and W_{CI} in Figure 7(c) are similar with each other. Each plot was fitted by an orthogonal reduced-major-axis fitting and the slopes and dispersion are summarized in Table 2. Each plot shows positive correlations with correlation coefficients of ~ 0.7 except for the early phase of W_{CO} vs. $N_{\text{HI}} + 2N_{\text{H}_2}$. W_{CO} is poorly correlated with $N_{\text{HI}} + 2N_{\text{H}_2}$ at 0.5 and 1.0 Myr, reflecting very low CO abundance (see Table 1)

In Figure 7 the intensities, W_{CO} and W_{CI} , are less than 20 K km s^{-1} and 1.3 K km s^{-1} , respectively, and the corresponding column density is less than $4 \times 10^{21} \text{ cm}^{-2}$ at epochs earlier than 1.0 Myr. We note that in the epoch 0.5 Myr, where the CO abundance is 10^{-6} , W_{CO} becomes $\sim 10 \text{ K km s}^{-1}$ and is observable by the current instruments. As seen in Table 1 the CO clouds in this phase is still dominated by H I, and H_2 abundance is about 10%.

4. DISCUSSION

4.1. Numerical simulations of the H I distribution and comparison with the H I and dust observations

Inoue & Inutsuka (2012) presented H_2 formation in converging H I flows which models the local interstellar H I gas, and calculated the three dimensional distribution of H_2 , CO, C I and C II as well as the gas density and pressure distributions at 0.02 pc resolution over a timescale of 10 Myr. Similar numerical simulations to Inoue & Inutsuka (2012) were made by the other authors including Glover & Mac Low (2007); Hennebelle et al. (2008); Valdivia & Hennebelle (2014); Valdivia et al. (2016). Glover & Mac Low (2007) assumes the CNM only in the initial state of the simulations. These authors calculated both for the static and turbulent initial velocity fields, and showed rapid molecular formation in the turbulent field. This work is different from Inoue & Inutsuka (2012) in that the UV shielding is effective from the beginning of

the simulations due to the high density CNM. In the simulations by [Hennebelle et al. \(2008\)](#), the chemical network is not incorporated, which is the major difference from [Inoue & Inutsuka \(2012\)](#). [Valdivia & Hennebelle \(2014\)](#); [Valdivia et al. \(2016\)](#) made follow up simulations with chemical reactions. [Valdivia et al. \(2016\)](#) argued that H₂ formation is rapid as compared with the static case, and found that H I is dominant as compared with H₂ in the early stage of evolution with $t < 10$ Myr. This trend is consistent with [Inoue & Inutsuka \(2012\)](#). [Kim et al. \(2013\)](#) made large-scale H I simulations in a galactic kpc-scale with lower spatial resolution of 2 pc, insufficient to resolve thermal instabilities.

[Inoue & Inutsuka \(2012\)](#) focused on the analysis of the basic gas physical properties such as energy and velocity, and showed the general trend of slow H₂ formation on dust surfaces and the dominant H I fraction over 10 Myr after the initiation of the H I flow collision. A confrontation of the predicted gas distributions with the observations was, however, beyond the scope of [Inoue & Inutsuka \(2012\)](#), and interpretation of the observations of H₂, CO and C I in a framework of [Inoue & Inutsuka \(2012\)](#) remained as a task for better understanding molecular cloud formation observationally.

As a step of applying the [Inoue & Inutsuka \(2012\)](#) results to the observations, [Fukui et al. \(2018\)](#) made a detailed visualization of the spatial distribution of H I and H₂ and compared the synthetic observational results with the observations of H I, the emission-absorption measurements toward radio continuum sources, and UV absorption measurements of H₂. An important outcome of [Fukui et al. \(2018\)](#) was the highly clumped distribution of the CNM, which occupies only 3–4% of the total volume. Such an extremely small filling factor of the CNM was not explicitly mentioned often in the literature, while qualitatively a small filling factor of the CNM was suggested previously (e.g., [Heiles & Troland 2003](#)). A usual understanding of the CNM and WNM is that the two have comparable mass and that the CNM is by a factor of 30 denser than the WNM. The ~ 30 times difference in average density between the CNM and WNM leads immediately to robust knowledge that the CNM volume filling factor is 3–4% of the WNM (e.g., see Table 1 of [Draine 2011](#)), and this is consistent with the synthetic observations of [Fukui et al. \(2018\)](#). As a general remark we need to be cautioned to use a “typical” value in calculating H I properties because the H I density and temperature have broad ranges over a few orders of magnitude with no clear peaks (Figure 1). Some typical value of H I thus sometimes can oversimplify the H I properties, and careful testing by considering distribution functions of the relevant parameters are required.

It could be questioned if the results of [Inoue & Inutsuka \(2012\)](#) may be a special situation caused by the continuous H I inflow which may produce too high pressure and too high CNM clumpiness (e.g., [Murray et al. 2018](#)). In order to test a possible model bias, we used several different models in the present work (Section 2). The new Models with different setups show a small volume filling factor of the CNM (Section 2 and Table 1), lending further support for the CNM small filling factor as a general

property of the interstellar H I. It is also to be noted that the gas distribution in the present simulations are all transient and is not in equilibrium. The clumps are not in pressure balance but changes in time by a typical timescale of $0.1 \text{ pc} / 3 \text{ km s}^{-1} \sim$ a few times 10^4 yr , and Figure 5 presents snapshots at each epoch. In this connection, the pressure of the ISM measured in the C I absorption (Jenkins & Tripp 2011) offers another possible test of the models. These authors derived $\log(p/k_b) = 3.58 \pm 0.175$ dex (rms) as the average pressure of the ISM based on the UV absorption of the ground state C I, where the rms error is a lower limit. Into more detail, their Figures 7 and 8 show a distribution function of $\log(p/k_b)$; all the data of $\log(p/k_b)$ have a broad range from 2.5 to 4.5 and the major portion is distributed from 3.0 to 4.2 for $dN(\text{H})/d(\log(p/k_b))$ above 10^{22} cm^{-2} . In the present model, C I samples mainly the low-density end, $\sim 10^2 \text{ cm}^{-3}$, of the CNM and its pressure weighted by C I mass is from 3.7 to 4.2, which is somewhat higher but is not inconsistent with the result of Jenkins & Tripp (2011).

Fukui et al. (2018) argued that the emission-absorption measurements usually underestimate the H I column density because the measurements bias toward the WNM which has a covering factor of 80% in the sky. Most of the emission-absorption measurements sample the optically thin WNM. Since the WNM has significantly small H I optical depth of $\sim 10^{-2}$ due to high spin temperature above 1000 K, the emission-absorption measurements biased toward the WNM underestimate the H I column density N_{HI} . On the other hand, the *Planck/IRAS*-based measurements (Fukui et al. 2014, 2015) derived larger N_{HI} than the emission-absorption measurements. The dust grains are included both in the CNM and WNM, and the dust emission samples the whole ISM volume. This difference in observational bias in the emission-absorption measurements explains the difference from the dust-based measurements. Fukui et al. (2018) in addition warned the extremely small area covering factor subtended by the radio continuum point-like sources used in the emission-absorption measurements which has density of one source every 10 square degrees in the sky, and argued that the emission-absorption measurements are not suited to derive bulk H I properties in the local ISM. A remaining issue to be better understood in the context is the dust property which was used as a proxy of hydrogen in the *Planck/IRAS* based method. Possible changes in dust emission properties need to be further carefully worked out. In this connection, Fukui et al. (2018) showed that the small dispersion of the optically thin regime, in the scatter plot between W_{HI} and τ_{353} , the dust optical depth at 353 GHz, is consistent with the uniform dust property, whereas a range of the dust optical depth is limited. It is noteworthy that, most recently, the dust optical depth as a proxy of the ISM is successfully applied to measure metallicity in the ISM in the Galactic halo and the Local Group galaxies (Fukui et al. 2017a,b).

4.2. The seed CO clouds and their observations

In the classical framework of molecular cloud formation, the density inhomogeneity and turbulence were not often considered in theoretical works (Dobbs et al. 2014). The present results, incorporating fully the turbulent inhomogeneities, show that the CNM distribution places the initial setup for H₂ formation, and H₂ formation proceed first in the heart of the CNM clumps in a time scale shorter than 1 Myr. We note that the H₂ abundance in the earliest phase $\lesssim 1$ Myr is as low as 10^{-1} at maximum in the CNM clumps and almost full conversion of H I into H₂ is realized at density 100 cm^{-3} in 10 Myr (Figure 4). In a timescale less than 3 Myr CO clouds are dominated by H I, and H I occupies more than 70% of hydrogen (see Figures 6(a)-1 and 6(b)-1 and Table 1). Such a picture of H I dominance in young CO clouds derived from the simulations by Inoue & Inutsuka (2012) is not usual in the literature. Fukui et al. (2018) showed that the CNM is distributed in small clumps whose size is in a sub-pc scale. The early spatial distribution of the CO clouds shows naturally highly clumpy distribution similar to the CNM (Tachihara et al. 2012; Fukui et al. 2018).

The present results predict the appearance of young CO clouds as clumpy H I dominated clouds of sub-pc size with low CO abundance of 10^{-8} to 10^{-6} even at their peak. Possible evidence for the seed CO cloud formation was reported in the Pegasus loop where an early B2 star HD 866 acted to compress the ambient H I gas into a shell of 30 pc radius at 250 pc distance (Yamamoto et al. 2006; distance 100 pc assumed by these authors is revised to 250 pc by Saeki et al. in prep. based on the new star count data). Small CO clouds of sub-pc to pc scales are distributed without massive CO cloud as revealed by the large scale CO $J = 1-0$ observations with NANTEN (Yamamoto et al. 2006). Yamamoto et al. (2006) paid attention to that the clouds show weak CO peak intensities of a few K which is unusual among the typical local dark clouds, and discussed that they may represent young CO clouds forming in shock compression by the B2 star within ~ 1 Myr. These authors compared the data with the cloud formation theory of Koyama & Inutsuka (2002), which is the earlier work of Inoue & Inutsuka (2012). In the Pegasus region the cloud mass ranges from $0.1 M_{\odot}$ to $50 M_{\odot}$ with a median of $5 M_{\odot}$, and most of them have radius less than 0.6 pc. These properties are consistent with the seed CO clouds in the present work.

Another region of similar small clouds in Ophiuchus was studied by Tachihara et al. (2012). These authors focused on a CO cloud named Cloud S (also known as LDN 204) in the Ophiuchus North region around an O9.5 star ζ Oph. The cloud was mapped in the CO $J = 1-0$ emission by the Nagoya 4 m mm-telescope (Nozawa et al. 1991) and NANTEN (Tachihara et al. 2000), and follow up higher resolution studies were made with the Nobeyama Radio Observaotry 45 m+BEARS receiver and ASTE 10 m telescopes in CO 1-0 and 3-2 emissions (Tachihara et al. 2012). These results showed small ¹²CO cloudlets having linewidth = 0.6 km s^{-1} , radius = 3000–6300 AU, mass = $0.005-0.05 M_{\odot}$, density = $(1-11) \times 10^3 \text{ cm}^{-6}$ and high $T_k = 25-300 \text{ K}$ irradiated by the O star. Most recently, new ALMA observation further resolved ¹²CO clouds having linewidth = 0.3 km s^{-1} , radius $\sim 1000 \text{ AU}$, and mass \sim

$10^{-4} M_{\odot}$, in Cloud S (Tachihara et al. in prep.). These results confirm very small scale distributions in the CO clouds, lending further support for the small structures predicted by the present study based on Inoue & Inutsuka (2012), while the ALMA resolution is higher than that of the current numerical simulations.

The present study also offers an insight into the later phase of CO cloud formation in particular at epochs after 3 Myr. The synthetic distributions suggest that small CO clouds likely merge into a large CO cloud by coagulation in a timescale longer than 3 Myr (Figure 6). A scenario of aggregation of small molecular clouds as a formation mechanism of large molecular clouds was presented theoretically (e.g., Dobbs et al. 2014; see also Pringle et al. 2001), whereas we are not aware of detailed numerical studies like the present one on the aggregation.

4.3. Similar pc-scale distributions of CO and C I

Some early C I data were taken by Maezawa et al. (1999); Ikeda et al. (1999); Kamegai et al. (2003) in local dark clouds and some more distant GMCs by Kramer et al. (2004), Burton et al. (2014) and Shimajiri et al. (2013). A common result of these studies is that two distributions of C I and CO are similar with each other in spite of that C I is formed in the less A_V layers than CO as shown by the PDR layered model by Tielens & Hollenbach (1985). According the PDR model, the C I layer with H I is at less than $A_V = 2$ mag and H₂ becomes dominant at A_V more than 2 mag where CO is still not abundant due to the less self-shielding of CO than H₂. The CO-dark H₂ layer is distributed at A_V between 2 mag and 3 mag (Tielens & Hollenbach 1985). H₂ with a CO layer follows this at more than $A_V = 3$ mag. $A_V = 1$ mag corresponds to $N_{\text{HI}} = 1.9 \times 10^{21} \text{ cm}^{-2}$ mag and in the layered model, the mass of the CO-dark H₂ may be significant. In the current picture of highly clumped C I and CO distribution, the CO-dark H₂ is in the surface of each clump and A_V to protect H₂ is a combination of A_V in the extended WNM and in the thin shell of the CNM clump. As a result, the mass fraction of CO-dark H₂ is negligibly small as shown in Table 3. It is not likely that the CO-dark H₂ is a major mass carrier in the local ISM, corresponding to only 1–2% of the total ISM mass. This is consistent with the similar spatial distribution of C I and CO observed in various clouds (Burton et al. 2014). The work by Glover et al. (2015) also explained the similar C I and CO distribution by a turbulent model which allows UV radiation to penetrate deeply into a cloud. The clumpy distribution of CO and C I provides a basis for the similarity between the CO and C I distributions averaged at a pc-scale. The present model shown in Figure 6 has $N_{\text{HI}} + 2N_{\text{H}_2} = (1\text{--}1.5) \times 10^{21} \text{ cm}^{-2}$, $N_{\text{HI,WNM}} = (0.3\text{--}0.5) \times 10^{21} \text{ cm}^{-2}$, and $N_{\text{HI,CNM}} = (0.2\text{--}1.1) \times 10^{21} \text{ cm}^{-2}$ (see also Table 5 of Fukui et al. 2018). This sightline does not include the peak of a CNM clump, where A_V , a sum of the WNM and CNM, can become as large as more than 2 mag which corresponds to A_V for the H I/H₂ transition. Because A_V of the WNM is somewhat smaller than that of the

CNM, UV radiation penetrates more deeply in the clumpy case than the layered case, allowing to produce C I throughout the ISM.

C I and CO are not extremely accurate tracers of the ISM as indicated by the relatively low correlation coefficients in the scatter plots W_{CO} vs. $N_{\text{HI}} + 2N_{\text{H}_2}$ or W_{CI} vs. $N_{\text{HI}} + 2N_{\text{H}_2}$ in Figure 7. For a given W_{CO} or W_{CI} , $N_{\text{HI}} + 2N_{\text{H}_2}$ is constrained typically within a factor of 2 as shown in Section 3. This large range is not inconsistent with the usual error range of a factor of 2 in X_{CO} , a conversion factor of W_{CO} into N_{H_2} (Okamoto et al. 2017). In the present Model setup, this is ascribed to the large variation of their abundance which changes with the local sub-pc scale conditions including UV radiation in each CNM clump. It is also noteworthy that H I is more abundant than H₂ at an age shorter than 10 Myr. Only after 10 Myr full conversion of H I into H₂ is realized where the H I abundance $\sim 10^{-2}$ (e.g., Sato & Fukui 1978) is primarily determined by the cosmic ray dissociation of H₂. The H I abundance in a CO cloud in its early evolutionary stages is dominated by non-equilibrium chemical reactions.

4.4. CO-dark H₂

Table 3 summarizes the mass budget of the ISM, H I and H₂, as probed by the usual tracers including CO and C I in the present study. In particular, the CO-dark H₂ has attracted attention as a possible important mass carrier in the ISM. It is argued that there is a significant amount of H₂ gas which is not detectable in CO emission. CO is dissociated by UV radiation at 11.2 eV, while H₂ is dissociated by UV radiation at 4.5 eV. H₂ is however more heavily protected than CO by self-shielding by its high abundance and a layer is formed where only H₂ is abundant and CO is much less, and undetectable. A theoretical model of the envelope of a GMC was presented by Wolfire et al. (2010) and showed that CO-dark H₂ has a significant fraction of gas mass. This model is however not aimed at simulating the local ISM which has more turbulent and transient properties in the solar neighborhood. In particular, the timescale of the model by Wolfire et al. (2010) is ~ 10 Myr and chemical equilibrium is assumed. This is not the case in the local ISM which is often disturbed by the SNR shocks in a 1 Myr scale as argued by Koyama & Inutsuka (2002, 2004). It is possible that CO-dark H₂ can be important in the GMCs, whereas it is not applicable to the transient local ISM which is the subject of the present study. The results in Table 3 show that the H₂ mass fraction is small, 10–30% at epochs 1–3 Myr and the fraction of the CO-dark H₂ is 10% of the total H₂ and only 1–2% of the total ISM. The CO-dark H₂ is therefore not likely as a dark mass candidate in the local ISM.

5. CONCLUSIONS

We carried out synthetic observations of the interstellar carbon in the forms of CO, C I and C II. The theoretical model based on magneto-hydrodynamical numerical simulations of H I gas converging at a velocity of 20 km s⁻¹ by Inoue & Inutsuka (2012) is employed. The gas is turbulent and inhomogeneous with magnetic field.

The model parameters at an epoch of 0.5 Myr were chosen to be consistent with the observations of H₂ in UV and 21 cm H I emission-absorption measurements of the local interstellar medium around the sun. We focus on the evolution of the rare species, CO, C I and C II, other than the main constituents H₂ and H I from 0.3 Myr to 9 Myr since the converging flow initiated interaction. We find two phases of cloud formation. In the early phase within 1 Myr, the CNM clumps of sub-pc scales are the formation sites of H₂, C I and CO, and in the late phase from 3 Myr to 9 Myr the CNM clumps merge together to form pc-scale molecular clouds. In the early phase the clumps are dominated by cool H I and the typical H₂ fraction is $\sim 10\%$ of H I, and the abundances of C I and CO are $\sim 10^{-5}$ of H₂. This predicts that the CO clumps in the early phase, the seed CO clouds, are detectable as sub-pc scale weak CO clouds. In the late phase the merged molecular clouds are dominated by H₂ where $n_{\text{H}_2}/(n_{\text{HI}} + 2n_{\text{H}_2}) \sim 0.1\text{--}1.0$ and the CO abundance reaches $\sim 10^{-4}$. These results are consistent with the large-scale observations of C I and CO, both of which show fairly similar spatial distributions due to the sub-pc clumpy distribution of C I and CO emitting regions. This makes a significant contrast with the classic picture of the PDR which predicted distinct pc-scale layers of C I and CO in the sequence of A_V (Tielens & Hollenbach 1985). We identified observational signatures of the molecular clouds in their infancy by low CO and high H I abundance where H₂ is yet minor species. We suggest that the faint CO clouds in the Ophiucus North (Tachihara et al. 2012) and the Pegasus loop (Yamamoto et al. 2006) are good candidates for such an early phase. We also note that the fraction of CO-dark H₂ is small, less than a few percent, and not important in the total mass budget of the local ISM which is dominated by the H I. This disagrees with the conventional idea that CO-dark H₂ is one of the major mass carriers in the ISM.

This work was supported by JSPS KAKENHI Grant Number JP15H05694.

REFERENCES

- Burton, M. G., Ashley, M. C. B., Braiding, C., et al. 2014, *ApJ*, 782, 72, doi: [10.1088/0004-637X/782/2/72](https://doi.org/10.1088/0004-637X/782/2/72)
- Dobbs, C. L., Krumholz, M. R., Ballesteros-Paredes, J., et al. 2014, *Protostars and Planets VI*, 3, doi: [10.2458/azu_uapress_9780816531240-ch001](https://doi.org/10.2458/azu_uapress_9780816531240-ch001)
- Draine, B. T. 2011, *Physics of the Interstellar and Intergalactic Medium*
- Dullemond, C. P., Juhasz, A., Pohl, A., et al. 2012, *RADMC-3D: A multi-purpose radiative transfer tool*, *Astrophysics Source Code Library*. <http://ascl.net/1202.015>
- Fukui, Y., Hayakawa, T., Inoue, T., et al. 2018, *ApJ*, 860, 33, doi: [10.3847/1538-4357/aac16c](https://doi.org/10.3847/1538-4357/aac16c)
- Fukui, Y., Torii, K., Onishi, T., et al. 2015, *ApJ*, 798, 6, doi: [10.1088/0004-637X/798/1/6](https://doi.org/10.1088/0004-637X/798/1/6)
- Fukui, Y., Tsuge, K., Sano, H., et al. 2017a, *PASJ*, 69, L5, doi: [10.1093/pasj/psx032](https://doi.org/10.1093/pasj/psx032)
- Fukui, Y., Okamoto, R., Kaji, R., et al. 2014, *ApJ*, 796, 59, doi: [10.1088/0004-637X/796/1/59](https://doi.org/10.1088/0004-637X/796/1/59)

- Fukui, Y., Koga, M., Maruyama, S., et al. 2017b, arXiv: 1711.09529, PASJ in press.
<https://arxiv.org/abs/1711.09529>
- Glover, S. C. O., Clark, P. C., Micic, M., & Molina, F. 2015, MNRAS, 448, 1607, doi: [10.1093/mnras/stu2699](https://doi.org/10.1093/mnras/stu2699)
- Glover, S. C. O., Federrath, C., Mac Low, M.-M., & Klessen, R. S. 2010, MNRAS, 404, 2, doi: [10.1111/j.1365-2966.2009.15718.x](https://doi.org/10.1111/j.1365-2966.2009.15718.x)
- Glover, S. C. O., & Mac Low, M.-M. 2007, ApJS, 169, 239, doi: [10.1086/512238](https://doi.org/10.1086/512238)
- Heiles, C., & Troland, T. H. 2003, ApJ, 586, 1067, doi: [10.1086/367828](https://doi.org/10.1086/367828)
- Hennebelle, P., Banerjee, R., Vázquez-Semadeni, E., Klessen, R. S., & Audit, E. 2008, A&A, 486, L43, doi: [10.1051/0004-6361:200810165](https://doi.org/10.1051/0004-6361:200810165)
- Hennebelle, P., Mac Low, M.-M., & Vázquez-Semadeni, E. 2009, Diffuse interstellar medium and the formation of molecular clouds, ed. G. Chabrier (Cambridge University Press), 205
- Ikeda, M., Maezawa, H., Ito, T., et al. 1999, ApJL, 527, L59, doi: [10.1086/312395](https://doi.org/10.1086/312395)
- Inoue, T., & Inutsuka, S.-i. 2012, ApJ, 759, 35, doi: [10.1088/0004-637X/759/1/35](https://doi.org/10.1088/0004-637X/759/1/35)
- Jenkins, E. B., & Tripp, T. M. 2011, ApJ, 734, 65, doi: [10.1088/0004-637X/734/1/65](https://doi.org/10.1088/0004-637X/734/1/65)
- Kamegai, K., Ikeda, M., Maezawa, H., et al. 2003, ApJ, 589, 378, doi: [10.1086/374352](https://doi.org/10.1086/374352)
- Kim, C.-G., Ostriker, E. C., & Kim, W.-T. 2013, ApJ, 776, 1, doi: [10.1088/0004-637X/776/1/1](https://doi.org/10.1088/0004-637X/776/1/1)
- Koyama, H., & Inutsuka, S.-i. 2002, ApJL, 564, L97, doi: [10.1086/338978](https://doi.org/10.1086/338978)
- . 2004, ApJL, 602, L25, doi: [10.1086/382478](https://doi.org/10.1086/382478)
- Kramer, C., Jakob, H., Mookerjee, B., et al. 2004, A&A, 424, 887, doi: [10.1051/0004-6361:20047085](https://doi.org/10.1051/0004-6361:20047085)
- Maezawa, H., Ikeda, M., Ito, T., et al. 1999, ApJL, 524, L129, doi: [10.1086/312316](https://doi.org/10.1086/312316)
- Murray, C. E., Peek, J. E. G., Lee, M.-Y., & Stanimirović, S. 2018, ApJ, 862, 131, doi: [10.3847/1538-4357/aacffe](https://doi.org/10.3847/1538-4357/aacffe)
- Nozawa, S., Mizuno, A., Teshima, Y., Ogawa, H., & Fukui, Y. 1991, ApJS, 77, 647, doi: [10.1086/191618](https://doi.org/10.1086/191618)
- Oka, T., Yamamoto, S., Iwata, M., et al. 2001, ApJ, 558, 176, doi: [10.1086/321536](https://doi.org/10.1086/321536)
- Okamoto, R., Yamamoto, H., Tachihara, K., et al. 2017, ApJ, 838, 132, doi: [10.3847/1538-4357/aa6747](https://doi.org/10.3847/1538-4357/aa6747)
- Pringle, J. E., Allen, R. J., & Lubow, S. H. 2001, MNRAS, 327, 663, doi: [10.1046/j.1365-8711.2001.04777.x](https://doi.org/10.1046/j.1365-8711.2001.04777.x)
- Sato, F., & Fukui, Y. 1978, AJ, 83, 1607, doi: [10.1086/112370](https://doi.org/10.1086/112370)
- Schöier, F. L., van der Tak, F. F. S., van Dishoeck, E. F., & Black, J. H. 2005, A&A, 432, 369, doi: [10.1051/0004-6361:20041729](https://doi.org/10.1051/0004-6361:20041729)
- Shimajiri, Y., Sakai, T., Tsukagoshi, T., et al. 2013, ApJL, 774, L20, doi: [10.1088/2041-8205/774/2/L20](https://doi.org/10.1088/2041-8205/774/2/L20)
- Tachihara, K., Abe, R., Onishi, T., Mizuno, A., & Fukui, Y. 2000, PASJ, 52, 1147, doi: [10.1093/pasj/52.6.1147](https://doi.org/10.1093/pasj/52.6.1147)
- Tachihara, K., Saigo, K., Higuchi, A. E., et al. 2012, ApJ, 754, 95, doi: [10.1088/0004-637X/754/2/95](https://doi.org/10.1088/0004-637X/754/2/95)
- Tielens, A. G. G. M., & Hollenbach, D. 1985, ApJ, 291, 722, doi: [10.1086/163111](https://doi.org/10.1086/163111)
- Valdivia, V., & Hennebelle, P. 2014, A&A, 571, A46, doi: [10.1051/0004-6361/201423720](https://doi.org/10.1051/0004-6361/201423720)
- Valdivia, V., Hennebelle, P., Génin, M., & Lesaffre, P. 2016, A&A, 587, A76, doi: [10.1051/0004-6361/201527325](https://doi.org/10.1051/0004-6361/201527325)
- Wolfire, M. G., Hollenbach, D., & McKee, C. F. 2010, ApJ, 716, 1191, doi: [10.1088/0004-637X/716/2/1191](https://doi.org/10.1088/0004-637X/716/2/1191)
- Yamamoto, H., Kawamura, A., Tachihara, K., et al. 2006, ApJ, 642, 307, doi: [10.1086/500797](https://doi.org/10.1086/500797)

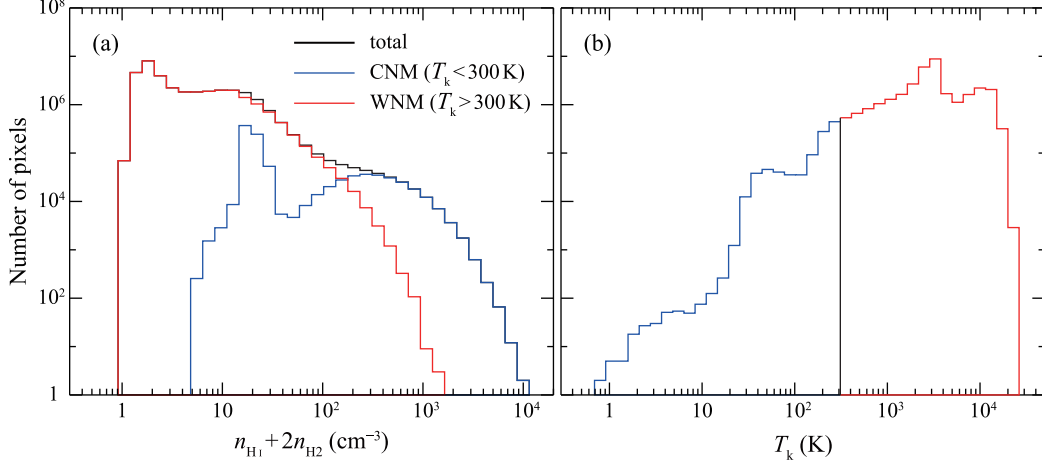


Figure 1. Histograms of (a) total hydrogen density ($n+2n_{\text{H}_2}$) and (b) kinetic temperature (T_k) for each pixel in Model A at 0.5 Myr (reproduced from Figure 5 of Fukui et al. 2018). The blue lines represent the contribution of $T_k < 300$ K and red lines represent that of $T_k > 300$ K.

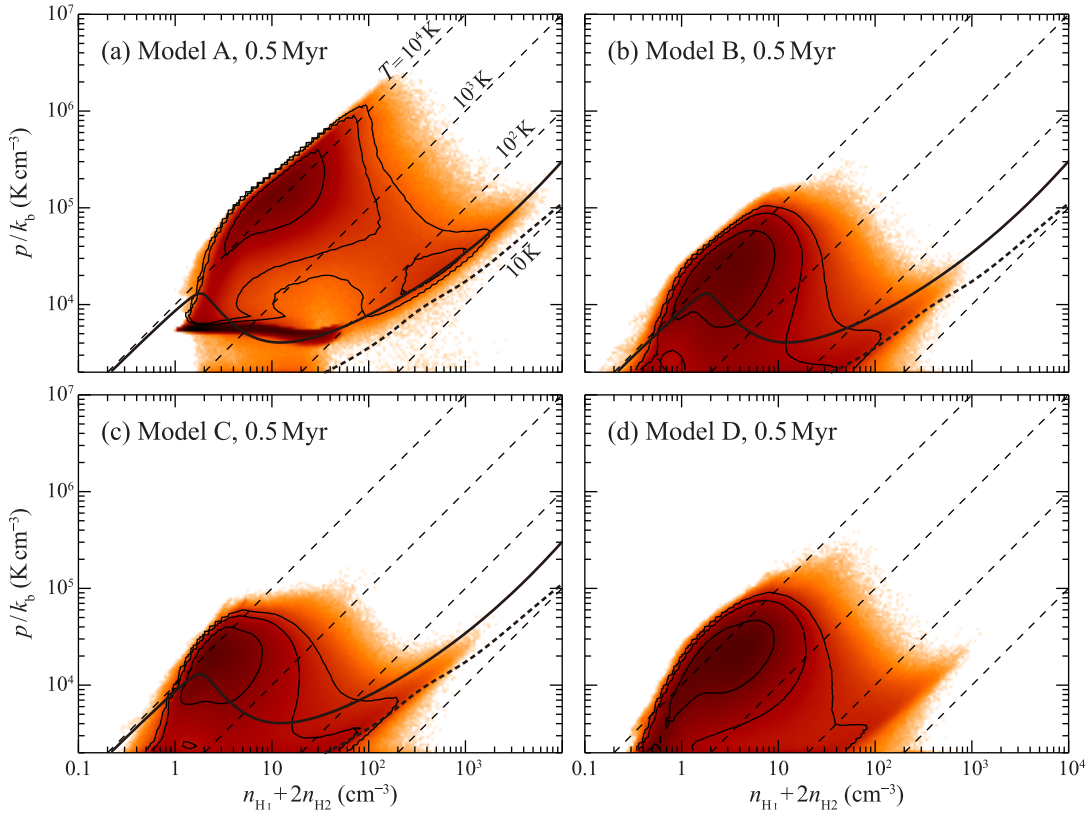


Figure 2. (a) Probability distribution function in the $(n_{\text{HI}} + 2n_{\text{H}_2})$ - p/k_b plane for Model A at 0.5 Myr. The condensation at $p/k_b \sim 7 \times 10^3 \text{ K cm}^{-3}$ shows the initial H I flows prior to the collision. The thick solid and dashed curves show thermal and chemical equilibrium curve for media of $A_V = 0 \text{ mag}$ and $A_V = 1 \text{ mag}$ (reproduced from Figure 1 of Inoue & Inutsuka 2012). The thin dashed lines are isotherms of $T_k = 10, 10^2, 10^3$ and 10^4 K . (b)–(d) Same as (a) but for Models B–D at 0.5 Myr.

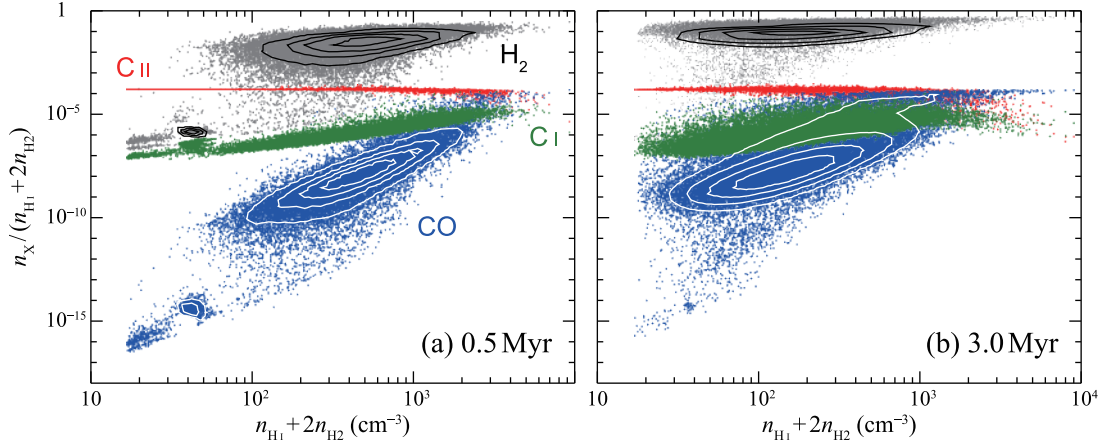


Figure 3. Relative abundance of H₂ (gray), CO (blue), C I (green), and C II (red) as a function of total density ($n_{\text{HI}} + 2n_{\text{H}_2}$) for pixels with $T_{\text{k}} < 100 \text{ K}$ in Model A at (a) 0.5 Myr and (b) 3.0 Myr. The black and white contours include 20%, 40%, 60% and 80% of H₂ data points and CO data points, respectively.

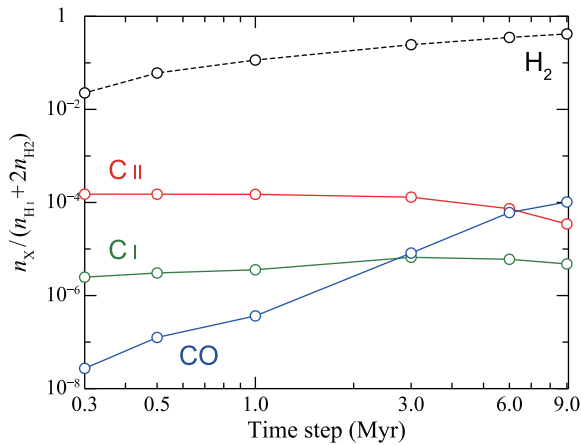


Figure 4. Time evolution of abundance of the four species of Model A measured at 10^3 cm^{-3} at epochs from 0.3 Myr to 9.0 Myr.

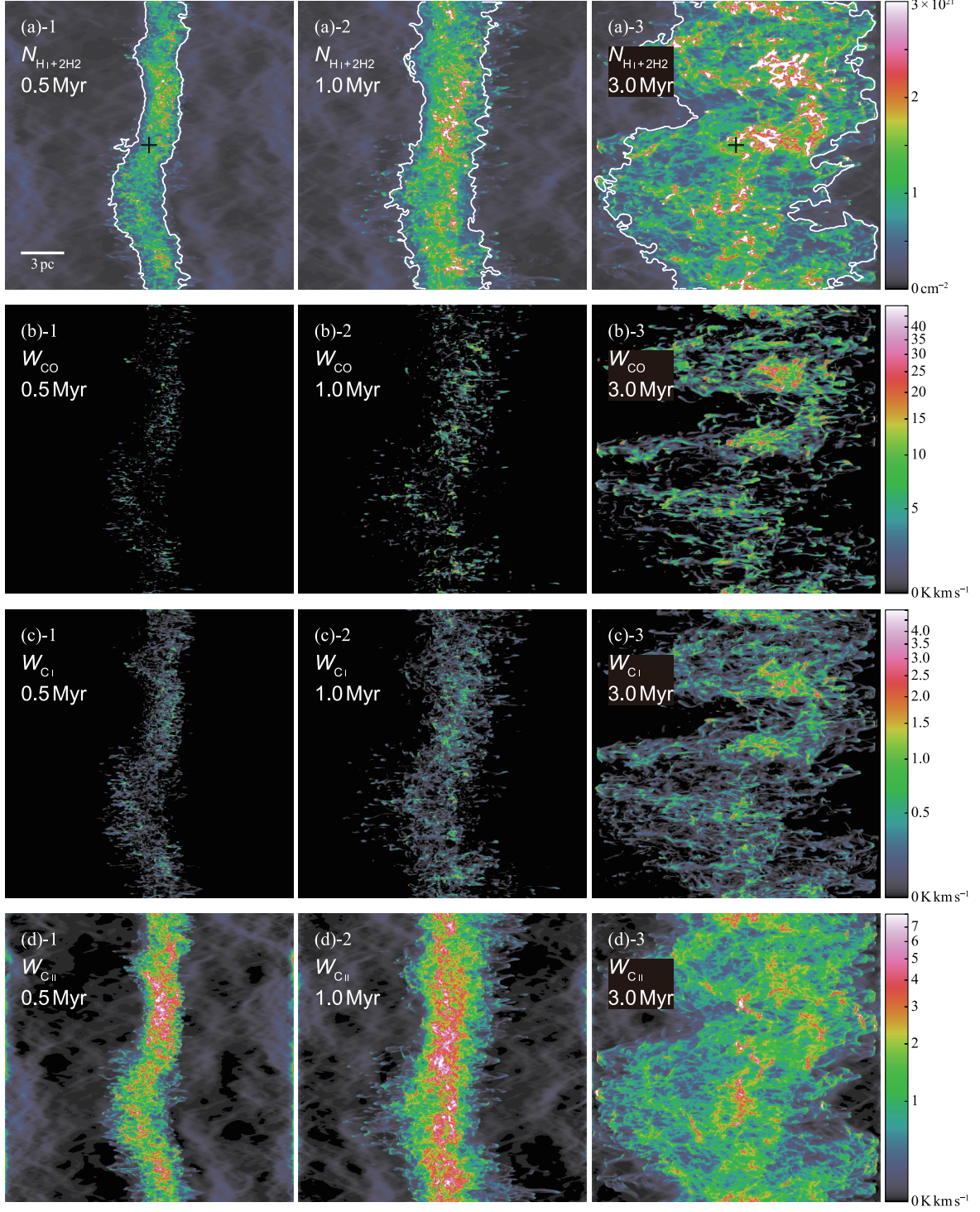


Figure 5. Spatial distribution of Model A at 0.5, 1.0 and 3.0 Myr (from left to right); (a) model total column density ($N_{\text{HI}} + 2N_{\text{H}_2}$), (b)–(d) velocity-integrated intensity of the synthetic observed CO, C I and C II. The images are 20 pc \times 20 pc in size and have a resolution of 0.04 pc per pixel. The x and z axes in the numerical domain correspond to the horizontal and the vertical axes in each panel.

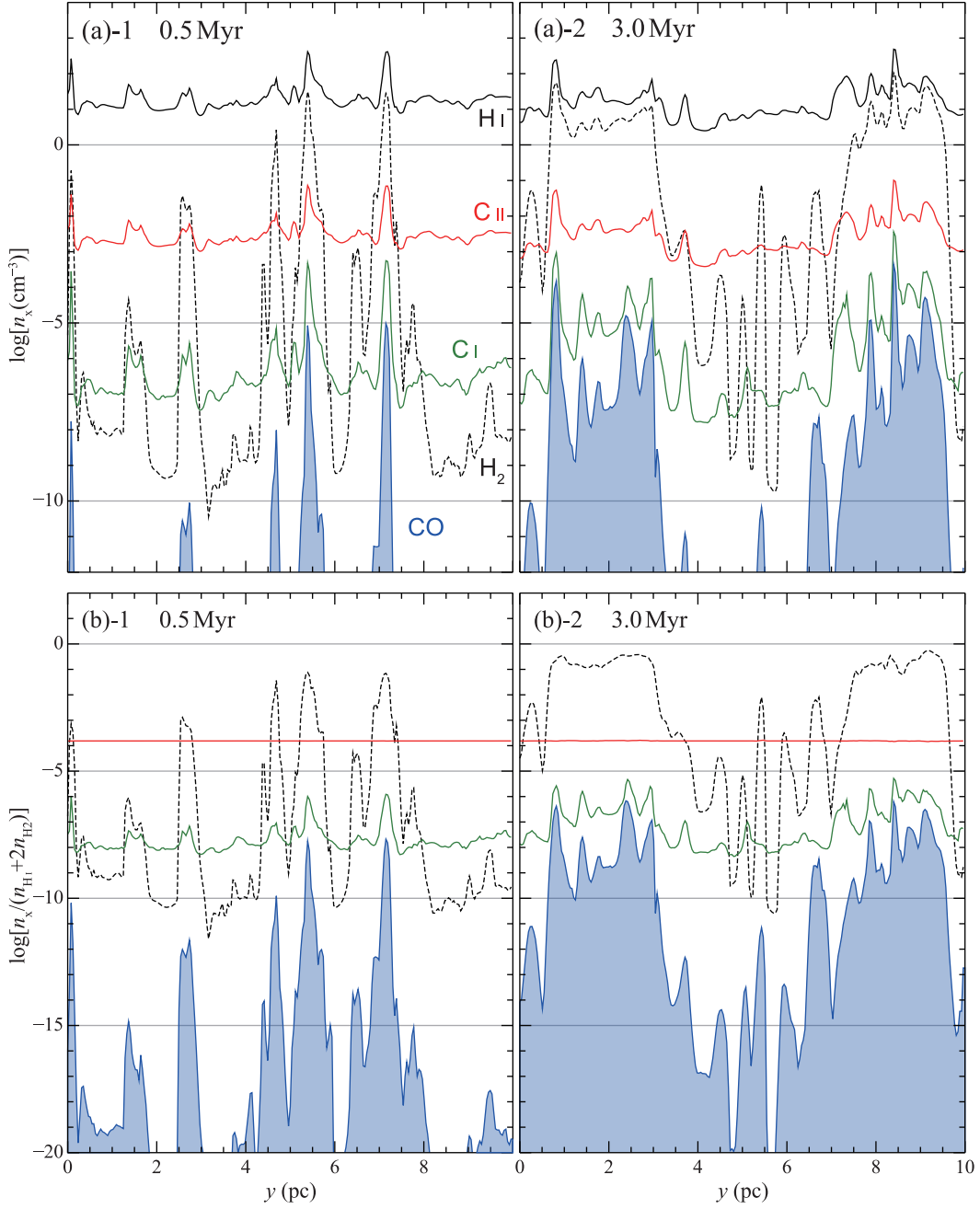


Figure 6. (a) Density n_X ($X=\text{H I}$, H_2 , C I , C II and CO) profiles in Model A at 0.5 Myr ((a)-1) along the line of sight toward the cross mark in Figure 5(a)-1, and at 3.0 Myr ((a)-2) toward the mark in Figure 5(a)-3. The horizontal axes are the distance from the far side of the model ISM, y . The black solid and dashed lines show H I and H_2 . The red, green and blue lines show C II , C I and CO , respectively. (b) Fraction $n_X / (n_{\text{HI}} + 2n_{\text{H}_2})$ profiles.

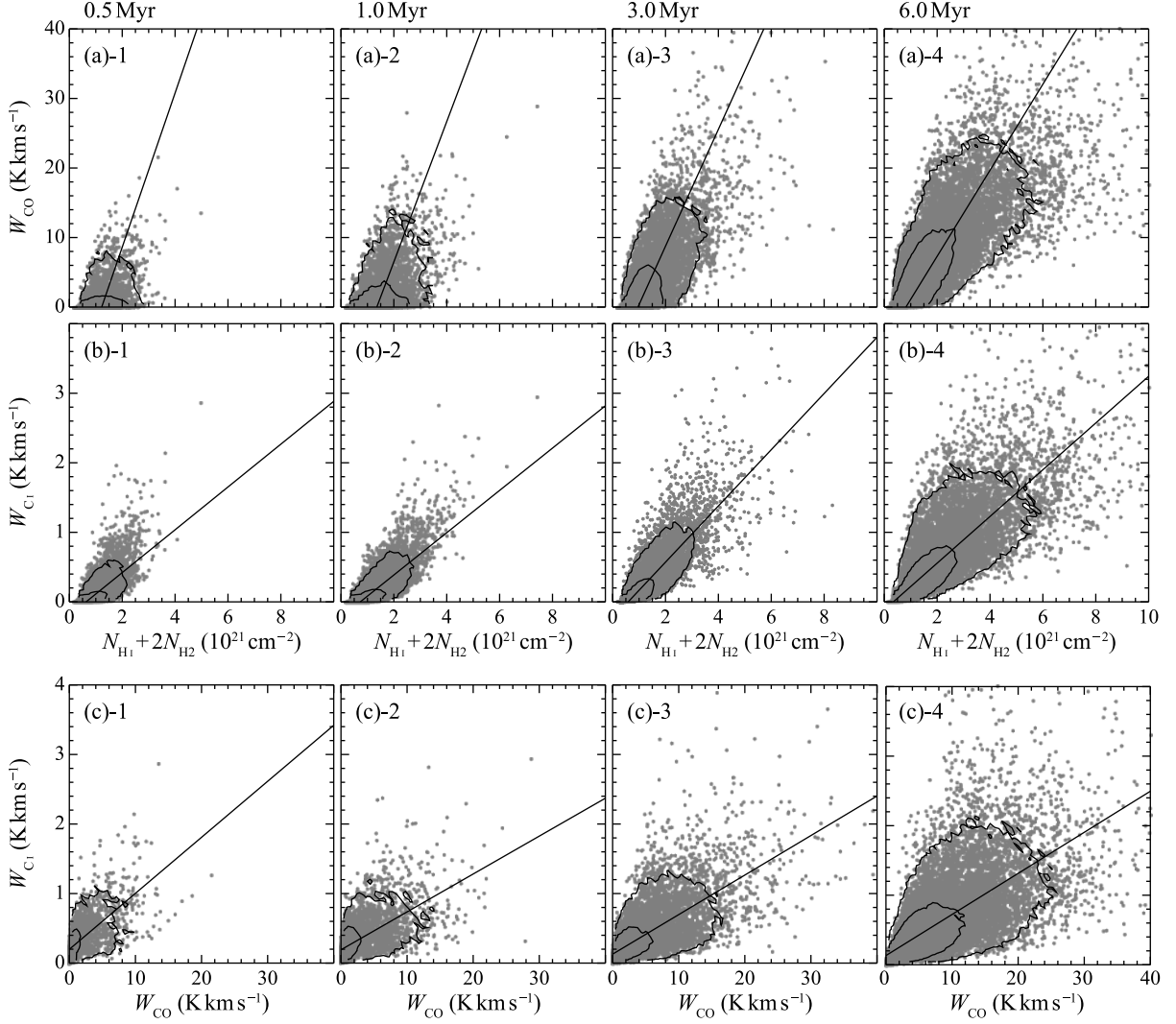


Figure 7. (a) Correlation plots of W_{CO} vs. $(N_{\text{HI}} + 2N_{\text{H}_2})$ in Modle I at 0.5, 1.0, 3.0 and 6.0 Myr (from left to right). (b) Those of W_{CI} vs. $(N_{\text{HI}} + 2N_{\text{H}_2})$ and (c) W_{CO} vs. W_{CI} . The contours include 70% and 95% of data points in each plot and the straight lines show linear regression line by orthogonal fitting (the slopes and dispersions are summarized in Table 2).

Table 1. Chemical abundance and the CNM volume filling factor

	Model A					Model B	Model C	Model D	
	0.3 Myr	0.5 Myr	1.0 Myr	3.0 Myr	6.0 Myr	9.0 Myr	0.5 Myr	0.5 Myr	0.5 Myr
$\log [n_X/(n_{\text{HI}} + 2n_{\text{H}_2})]^a$ (X=H ₂ , C II, C I, CO)									
H ₂	-1.6	-1.2	-0.9	-0.6	-0.5	-0.4	-1.3	-1.2	-1.4
C II	-3.8	-3.8	-3.8	-3.9	-4.1	-4.5	-3.9	-3.9	-3.9
C I	-5.6	-5.5	-5.4	-5.2	-5.2	-5.3	-4.6	-4.8	-4.8
CO	-7.6	-6.9	-6.4	-5.0	-4.2	-4.0	-5.1	-5.4	-5.9
CNM volume filling factor									
	3.4%	3.5%	5.0%	12.6%	29.0%	37.2%	4.4%	6.5%	2.4%

^aDecimal logarithm of median relative abundance, measured in a $(n_{\text{HI}} + 2n_{\text{H}_2})$ range from $10^{2.9}$ to $10^{3.1} \text{ cm}^{-3}$.

Table 2. Fitting results in the scatter plots of W_{CO} , W_{CI} and $(n_{\text{HI}} + 2n_{\text{H}_2})$

Time step (Myr)	<i>A</i>	<i>B</i>	C.C.
(1)	(2)	(3)	(4)
$W_{\text{CO}}(\text{K km s}^{-1}) = A(N_{\text{HI}} + 2N_{\text{H}_2})(10^{21} \text{ cm}^{-2}) + B$			
0.5	11.1 ± 0.5	-13.6 ± 0.6	0.36
1.0	10.1 ± 0.2	-13.7 ± 0.3	0.48
3.0	8.40 ± 0.06	-8.05 ± 0.07	0.71
6.0	6.19 ± 0.03	-5.07 ± 0.04	0.76
$W_{\text{CI}}(\text{K km s}^{-1}) = A(N_{\text{HI}} + 2N_{\text{H}_2})(10^{21} \text{ cm}^{-2}) + B$			
0.5	0.308 ± 0.005	-0.195 ± 0.005	0.67
1.0	0.304 ± 0.003	-0.222 ± 0.003	0.76
3.0	0.404 ± 0.002	-0.238 ± 0.002	0.82
6.0	0.336 ± 0.002	-0.115 ± 0.003	0.79
$W_{\text{CI}}(\text{K km s}^{-1}) = AW_{\text{CO}}(\text{K km s}^{-1}) + B$			
0.5	0.081 ± 0.002	0.198 ± 0.003	0.69
1.0	0.0545 ± 0.0009	0.191 ± 0.002	0.67
3.0	0.0568 ± 0.0004	0.129 ± 0.001	0.73
6.0	0.0591 ± 0.0003	0.133 ± 0.001	0.70

NOTE— Columns: (2) slope and (3) intercept of orthogonal reduced-major-axis regression line, (4) correlation coefficient.

Table 3. Mass budget

Time step (Myr)	$M_{\text{HI}} + M_{\text{H}_2}$ (M_{\odot})	M_{HI} (M_{\odot})	$M_{\text{HI}}^{\text{thin}}$ (M_{\odot})	M_{H_2} (M_{\odot})	$M_{\text{H}_2}^{\text{CO}}$ (M_{\odot})	$M_{\text{H}_2}^{\text{CO-free}}$ (M_{\odot})
(1)	(2)	(3)	(4)	(5)	(6)	(7)
0.3	269	265	205	5	2	3
		[98%]	[76%]	[2%]	[1%]	[1%]
0.5	413	394	310	19	12	7
		[95%]	[75%]	[5%]	[3%]	[2%]
1.0	820	746	564	75	64	11
		[91%]	[69%]	[9%]	[8%]	[1%]
3.0	2392	1732	1115	661	613	48
		[72%]	[47%]	[28%]	[26%]	[2%]
6.0	4754	2324	1191	2430	2401	29
		[49%]	[25%]	[51%]	[51%]	[1%]
9.0	6406	2028	992	4377	4367	10
		[32%]	[15%]	[68%]	[68%]	[0.1%]

NOTE— Columns: (2) total mass of H I and H₂, (3) mass of H I gas, (4) mass of H I given from H I integrated intensity under the optically thin assumption, (5) mass of H₂, (6) mass of H₂ detected by the synthetic CO observation (see Section 2) with detection limit of $W_{\text{CO}} > 0.1 \text{ K km s}^{-1}$, (7) mass of H₂ not detected by the synthetic CO observation.